Advection modes by optimal mass transfer

Angelo Iollo*
Institut de Mathématiques de Bordeaux, UMR 5251 CNRS, Université de Bordeaux, Inria Bordeaux, Sud Ouest, 33400 Talence, France

Damiano Lombardi†
Inria Paris-Rocquencourt, B.P. 105 Domaine de Voluceau, 78153 Le Chesnay, France
(Received 13 December 2013; published 24 February 2014)

Classical model reduction techniques approximate the solution of a physical model by a limited number of global modes. These modes are usually determined by variants of principal component analysis. Global modes can lead to reduced models that perform well in terms of stability and accuracy. However, when the physics of the model is mainly characterized by advection, the nonlocal representation of the solution by global modes essentially reduces to a Fourier expansion. In this paper we describe a method to determine a low-order representation of advection. This method is based on the solution of Monge-Kantorovich mass transfer problems. Examples of application to point vortex scattering, Korteweg–de Vries equation, and hurricane Dean advection are discussed.

DOI: 10.1103/PhysRevE.89.022923 PACS number(s): 05.45.−a, 47.90.+a, 47.11.−j

I. INTRODUCTION

Principal component analysis (PCA) is the main tool behind many techniques to perform model reduction of systems of partial differential equations (PDEs). The objective of model reduction is to obtain a simpler model that retains the main dynamical features of the full model, typically for optimization and control purposes. The principle of PCA is to find the base of a small dimensional subspace in such a way that the solution of a given PDE is accurately represented in this subspace. This is the main idea behind proper orthogonal decomposition (POD) [1,2]: for a given database of model solutions, POD extracts a basis that minimizes the L^2 average distance between the reduced representation and the solution database. POD approximations are usually satisfactory for those problems where the solution has a global behavior or is periodic [3], but perform poorly for systems characterized by concentrated structures that are advected. The main reason for this is that a simple shift cannot be represented by a linear combination of global modes.

Alternatives to POD taking implicitly into account the notion of transport in the definition of a global reduced basis are provided by Koopman modes [4,5] and dynamic mode decomposition (DMD) [6]. These approaches assume the existence of a linear propagator (relative to some possibly nonlinear map) whose spectrum provides a frequency-based mode decomposition of the considered evolution. Starting from snapshots of some observables of the physical system, an Arnoldi-type algorithm is employed to estimate the linear propagator.

Our objective is different. We introduce the notion of advection modes: when advection is the leading phenomenon, a hierarchy of advection modes can adequately approximate the evolution of coherent structures. Let us see how in two steps.

A. Transport

In Fig. 1 a conceptual description of transport is shown. Given a point $\xi \in \Omega_0$, where $\Omega_0 \subset \mathbb{R}^d$ is the reference configuration, transport at time t is described by a mapping $X(\xi,t)$. The point $x = X(\xi,t)$ belongs to the physical configuration $\Omega \subset \mathbb{R}^d$ at time t. Let us consider a point x in the actual physical configuration. The inverse mapping, $\xi = Y(x,t)$ (called otherwise backward characteristics), identifies the point in the reference configuration that has been transported by the direct map in x at time t.

The following relations hold:

$$Y = X^{-1}, \;\; [\nabla_\xi X][\nabla_x Y] = I, \tag{1}$$

where $[\nabla_\xi X]$ is the Jacobian of the transformation $X(\xi,t)$ and $[\nabla_x Y]$ its inverse, i.e., the Jacobian of the inverse mapping. Also, we have

$$\partial_t Y + \mathbf{v} \cdot \nabla_x Y = 0, \;\; Y(x,0) = x, \tag{2}$$

$$\mathbf{v} = \partial_t X, \;\; X(\xi,0) = \xi, \tag{3}$$

where $\mathbf{v}$ is the velocity field. Transport is uniquely determined by $\mathbf{v}(x,t)$ or equivalently by $\partial_t X(\xi,t)$.

Let us now consider a transport purely governed by advection. The nonlinear advection equation

$$\partial_t \mathbf{v} + \mathbf{v} \cdot \nabla_x \mathbf{v} = 0 \tag{4}$$

with $\mathbf{v}(x,0) = \mathbf{v}_0(x)$, can be interpreted as a model for a pressureless Euler flow. Since no force is acting on the fluid, the velocity is constant along the characteristics and the solution consists of particles moving on straight lines (no acceleration) determined by the initial transport velocity. In Lagrangian coordinates we have ($x = \xi$ for $t = 0$)

$$\partial_t^2 X(\xi,t) = 0 \implies X(\xi,t) = \xi + \mathbf{v}_0(\xi)\, t. \tag{5}$$

B. Optimal transport

Let us consider the following problem of mass transportation: two densities of equal mass are given, namely ϱ_0 and ϱ_1,

*angelo.iollo@math.u-bordeaux1.fr
†damiano.lombardi@inria.fr

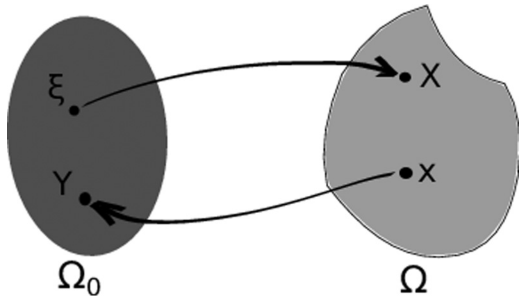

FIG. 1. The reference configuration is Ω_0, points $\xi \in \Omega_0$ are transported by the direct mapping in $X(\xi,t)$. Given the actual configuration Ω, a point $x \in \Omega$ is sent back to its counterimage in the reference configuration by backward characteristics, i.e., the inverse mapping $Y(x,t)$.

defined in the initial ($\xi \in \Omega_0$) and in the final configuration [$x = X(\xi,t=1) \in \Omega_1$]. The mass is normalized so that

$$\int_{\Omega_0} \varrho_0(\xi)\, d\xi = \int_{\Omega_1} \varrho_1(x)\, dx = 1. \tag{6}$$

The objective is to find the mapping $X(\xi)$ that transports ϱ_0 into ϱ_1. To this end, let us first rewrite the mass conservation equation by using the mapping definition $x = X(\xi)$:

$$\int_{\Omega_0} \varrho_0(\xi)\, d\xi = \int_{\Omega_0} \varrho_1(X(\xi)) \det(\nabla_\xi X)\, d\xi, \tag{7}$$

that, for $X(\xi)$ one to one, may be recast as

$$\varrho_0(\xi) d\,\xi = \varrho_1(X(\xi)) \det(\nabla_\xi X), \tag{8}$$

which is the Jacobian equation, accounting for mass conservation from a Lagrangian standpoint. The solution of the Jacobian equation is not unique. Among all the mappings satisfying the Jacobian equation, the optimal mapping is defined as the one that minimizes:

$$\mathcal{J} = \int_{\Omega_0} \varrho_0 |X(\xi) - \xi|^2\, d\xi. \tag{9}$$

The problem of finding the minimizer of this cost under the mass conservation constraint is called the L^2 Monge-Kantorovich problem. It is proved that the solution exists unique and it is of the form $X(\xi) = \nabla_\xi \Phi(\xi)$, where Φ is convex almost everywhere in the sense of measures. Other costs have been proposed in the literature, and we refer to [7] for a comprehensive review of the topic.

The solution of the optimal mass transport problem defines naturally a distance between density pairs, which is the Wasserstein distance:

$$\mathcal{W}^2(\varrho_i,\varrho_j) = \inf_{\tilde{X}} \left\{ \int_{\Omega} \varrho_i(\xi) |\tilde{X}(\xi) - \xi|^2\, d\xi \right\}, \quad \text{subject to} \tag{10}$$

$$\varrho_i(\xi) = \varrho_j(\tilde{X}(\xi)) \det(\nabla_\xi \tilde{X}). \tag{11}$$

It is worth noting that the problem of L^2 Monge-Kantorovich optimal transport may be formulated in an Eulerian framework (i.e., the Benamou-Brenier formulation; see for instance [8]). By introducing the time t, so that $x = X(\xi,t)$,

$$(\tilde{\varrho},\tilde{v}) = \arg\min_{\varrho,v} \left\{ \int_0^1 \int_\Omega \frac{1}{2}\varrho v^2 + \lambda(\partial_t \varrho + \nabla \cdot (\varrho v))\, d\Omega\, dt \right\}, \tag{12}$$

whose solution is the couple $(\tilde{\varrho}(x,t),\tilde{v}(x,t))$ satisfying a pressureless Euler flow, with prescribed initial and final density configurations.

The principle of the method is to represent subsequent instances of a given field (the snapshots) as the mapping of a reference distribution. The mapping is defined by a combination of pure advection transports. If the snapshots cannot be described by purely advected structures, we represent the residual fields by empirical global modes.

The physical reason for which this approach should lead to more accurate low-dimensional representations compared to POD is that fluid flows often present characteristic features that are mainly advected and then diffused, e.g., vorticity, solitary waves, shocks waves. Here we propose a modal expansion taking into account these two basic mechanisms via a representation that is adapted to each of them. Advection will be described by a ranked sequence of mappings and diffusion by a ranked global mode expansion. Each ranking is based on an appropriate error norm. This representation respects both these mechanisms (advection and diffusion) contrary to a sole global modal expansion like in POD.

C. Global modes and transport modes

A modal decomposition of a flow field can be obtained by defining an optimal approximation subspace of given size. Given a sequence of flow-field snapshots, this is usually done by minimizing the difference between one snapshot and its projection in the subspace to be determined. Let $u(x,t)$ be a scalar quantity relative to the flow field, and $\hat{u}(x,t)$, $\tilde{u}(x,t)$ two (small dimensional) approximations of such a scalar.

With POD, the difference to be minimized is defined by an appropriate norm and the flow field is represented by

$$\hat{u}(x,t) = \sum_i a_i(t)\varphi_i(x), \tag{13}$$

where the function φ_i is called the ith POD mode and is computed as a linear combination of the snapshots. The POD modes are global fields, i.e., defined everywhere in the actual physical configuration.

For advection mode decomposition the principle is different. We take

$$\tilde{u}(x,t) = [u_0(Y(x,t)) + R(Y(x,t),t)] \det(\nabla_x Y(x,t)), \tag{14}$$

where $u_0(\xi)$ is a reference mode that is mapped by $Y(x,t)$ and $R(\xi,t)$ is the residual in the reference configuration. The equivalent of this representation in the reference configuration is

$$u_0(\xi) = \tilde{u}(X(\xi,t),t) \det(\nabla_\xi X(\xi,t)) - R(\xi,t). \tag{15}$$

The main idea is to give a small-dimensional expansion of the mapping $X(\xi,t)$ and of the residual $R(\xi,t)$ such that

$$R(\xi,t) = \sum_j \alpha_j(t)\varphi_j(\xi), \tag{16}$$

$$X(\xi,t) = \sum_k \beta_k(t)\Phi_k(\xi), \tag{17}$$

where $\alpha_j(t)$ and $\beta_k(t)$ are time dependent scalars, $\varphi_j(\xi)$ are POD modes for the residual R, and $\Phi_k(\xi)$ are the advection modes to be found as explained in the following.

II. ADVECTION MODE DECOMPOSITION

In this section we explain how to determine the reference (or barycentral) mode $u_0(\xi)$, the advection modes, and the residual modes starting from a snapshot set.

The modal decomposition for the advection may be determined by setting up an approximated principal component analysis based on the Wasserstein distance. When performing this operation, the modes are vector fields realizing an optimal transport.

A. Euclidean embedding

The squared Wasserstein distance can be computed for all $i,j = 1,\dots,N_s$, i.e., $\frac{1}{2}N_s(N_s-1)$ Monge-Kantorovich problems are solved. Then, the following matrix $D \in \mathbb{R}^{N_s\times N_s}$ is defined:

$$D = \{\mathcal{D}_{ij}\} = \{\mathcal{W}^2(\varrho_i,\varrho_j)\}, \tag{18}$$

that is, the matrix of the squared distances between the densities. This matrix is symmetric $[\mathcal{W}(\varrho_i,\varrho_j) = \mathcal{W}(\varrho_j,\varrho_i)]$ and all the elements on the diagonal are zero $[\mathcal{W}(\varrho_i,\varrho_i) = 0]$.

In an Euclidean vector space, one can uniquely transform a matrix of canonical squared distances relative to a set of points, in a positive semidefinite matrix whose entries are the corresponding scalar products between the position vectors χ_i, $i = 1,\dots,N_s$, of those points. In other words

$$\mathcal{D}_{ij} = \|\chi_i - \chi_j\|^2 = \mathcal{B}_{ii} + \mathcal{B}_{jj} - 2\mathcal{B}_{ij}, \tag{19}$$

where $\mathcal{B}_{ij} = \chi_i \cdot \chi_j$ are the entries of a matrix $B \in \mathbb{R}^{N_s\times N_s}$. Let $\chi_i \in E \subset \mathbb{R}^{N_s}$ and let $\mathbf{1} \in \mathbb{R}^{N_s}$ be a column vector whose components are all 1. We assume that the origin of the vector space is such that $\sum_{i=1}^{N_s}\chi_i = 0$ and hence that $B\,\mathbf{1} = 0$. Then Eq. (19) can be inverted and we have

$$B = -\tfrac{1}{2}JDJ \tag{20}$$

and

$$J = I - \frac{1}{N_s}\mathbf{1}\mathbf{1}^T, \tag{21}$$

where I is the identity matrix. We assumed that E is an Euclidean space. In this case it can be shown that Eq. (20) leads to a matrix B that is positive semidefinite.

For a Wasserstein distance matrix this is not necessarily the case. However, one can look for a Euclidean set of vectors that gives a squared distance matrix which is an approximation of the Wasserstein square distance matrix. In order to do this, we adopt the same technique presented in [9].

Matrix B is real and symmetric and hence it can be decomposed as

$$B = USU^T, \tag{22}$$

where $U, S \in \mathbb{R}^{N_s\times N_s}$, U is a unitary matrix, and S is the diagonal matrix whose entries are the eigenvalues of B. Let us take the positive part of B,

$$B^+ = US^+U^T \text{ where } S^+ = \frac{S+|S|}{2} \tag{23}$$

so that $D \approx B^+$, $\|D - B^+\| = \|\frac{S-|S|}{2}\|$, and B^+ is of course positive semidefinite. It is now possible to determine matrix $\mathcal{X}$ whose columns are the position vectors χ_i as $\mathcal{X} = \sqrt{S^+}\,U^T$. In the Appendix we discuss a normalization technique relative

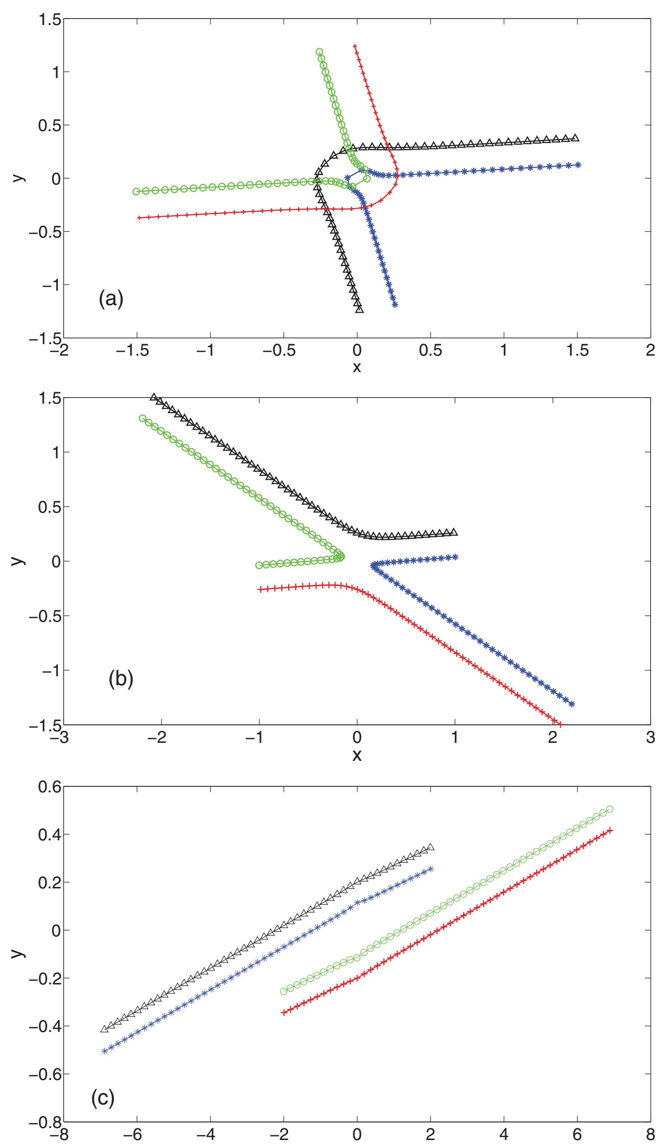

FIG. 2. (Color online) Three different scattering trajectories of vortex cores for (a) $l = 1.5$, $\beta = 0.5$, $f = 0.25$; (b) $l = 1.0$, $\beta = 0.75$, $f = 0.15$; (c) $l = 2.0$, $\beta = 0.15$, $f = 0.30$.

to this embedding which is useful when a large number of snapshots are considered.

In synthesis we have determined a Euclidean space where the flow snapshots are represented by points whose relative Euclidean distance approximates their Wasserstein distance. Moreover, linear combinations of vectors in this Euclidean space correspond to linear combinations of transports. The main approximation is that linear combinations of optimal transports are not optimal. A measure of this nonoptimality is $\|D - B^+\|$.

B. Advection modes

As stated, the embedding is performed with respect to the barycentral density distribution $u_0(\xi)$. The vector χ_i represents the position in phase space of the ith flow snapshot with respect to this density distribution. The advection modes are simply defined as the optimal transports corresponding to a base of this space. We refine this idea hereafter.

A small-dimensional representation of the space spanned by the position vectors χ can be found if the spectrum of B^+ rapidly decays to 0, i.e., S^+ has only a few diagonal nonzero entries. For example, assume that only the largest N_t eigenvalues of S^+ are retained and that the others are set to 0. Also, consider a canonical base of $\mathbb{R}^{N_t}$ and let $\bar{\chi}_i$ be the expression of vectors χ_i in this space. The components of $\bar{\chi}_i$ are simply the first N_t components of χ_i.

Let us take any point $\bar{\chi}_\alpha$ and choose N_t linearly independent vectors among the $N_s - 1$ vectors $\chi_i - \chi_\alpha$, such that $i \neq \alpha$. The origin of $\mathbb{R}^{N_t}$ can be expressed in this base thanks to N_t uniquely defined scalar coefficients $\{\beta_1, \beta_2, \ldots, \beta_{N_t}\}$.

We define the mapping that transports ϱ_α in the barycentral density u_0 as

$$X_o(\xi) = \sum_{i=1}^{N_t} \beta_i X_{\alpha\, i}(\xi), \tag{24}$$

where $X_{\alpha\, i}(\xi)$ denotes the mapping that transports ϱ_α onto ϱ_i. In consequence, u_0 can be found by

$$u_0(X_o(\xi)) = \frac{\varrho_\alpha(\xi)}{\det(\nabla_\xi X_o(\xi))}. \tag{25}$$

The advection modes are found as the optimal transports $X_{o\, i}(\xi)$ between $u_0(\xi)$ and the snapshots corresponding to linearly independent χ_i, i.e., snapshots that are not connected by the same transport. Thus, N_t advection modes are defined as $\Phi_i(\xi) = X_{o\, i}(\xi)$.

C. Residual representation

Let the flow-field snapshots correspond to a time-dependent phenomenon and let each snapshot be relative to time t_i. We define the following residual fields:

$$\begin{aligned} R_i(\xi) &= R_i(X(\xi,t_i)) \\ &= u(X(\xi,t_i),t_i)\det(\nabla_\xi X(\xi,t_i)) - u_0(\xi), \end{aligned} \tag{26}$$

where $u(x,t_i) = u(X(\xi,t_i),t_i)$ are the solution snapshots,

$$X(\xi,t_i) = \beta_j(t_i)\Phi_j(\xi), \tag{27}$$

and the coefficients $\beta_j(t_i)$ are the components of χ_i in the base of the space spanned by the advection modes.

The residual is approximated by a global mode expansion based on POD modes. The elements of the correlation matrix $A = \{\mathcal{A}_{ij}\}$ are defined by

$$\mathcal{A}_{ij} = \int_{\Omega_0} R_i(\xi)\, R_j(\xi)\, d\xi, \tag{28}$$

and the POD residual modes are determined through the eigenvalues and eigenvectors of the autocorrelation matrix:

$$\varphi_k(\xi) = \frac{\sum_{h=1}^{N_s} b_h^k R_h(\xi)}{\lambda_k^{1/2}}, \tag{29}$$

where b_h^k is the hth component of the kth eigenvector of A and λ_k its corresponding eigenvector.

We finally obtained a representation in a reference configuration of a time dependent field, decomposed in a mean field (the barycentral density or equivalently the initial condition) and a POD expansion.

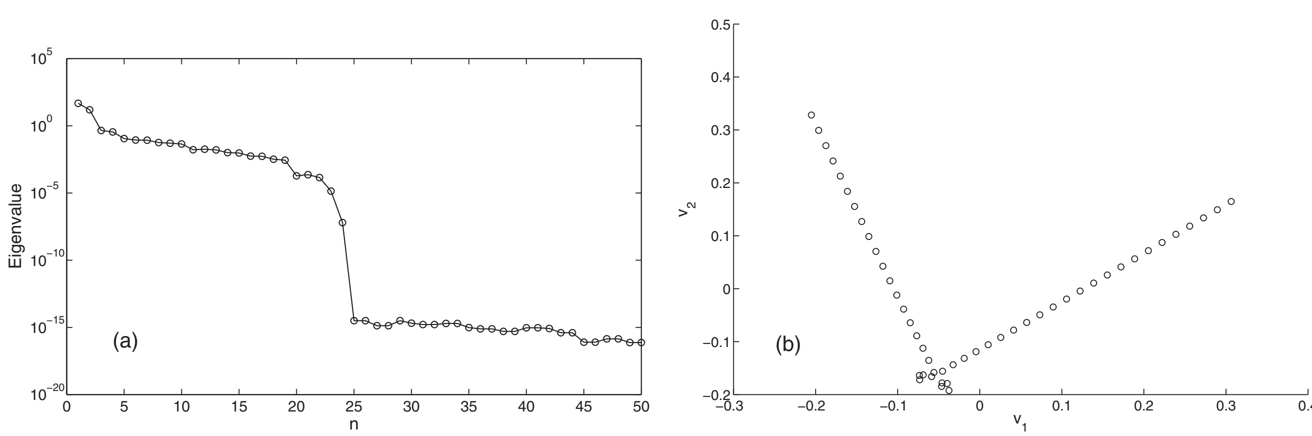

FIG. 3. First case: (a) the eigenvalues of the embedding matrix in logarithmic scale; (b) the first two eigenvectors are represented in a phase-plane plot.

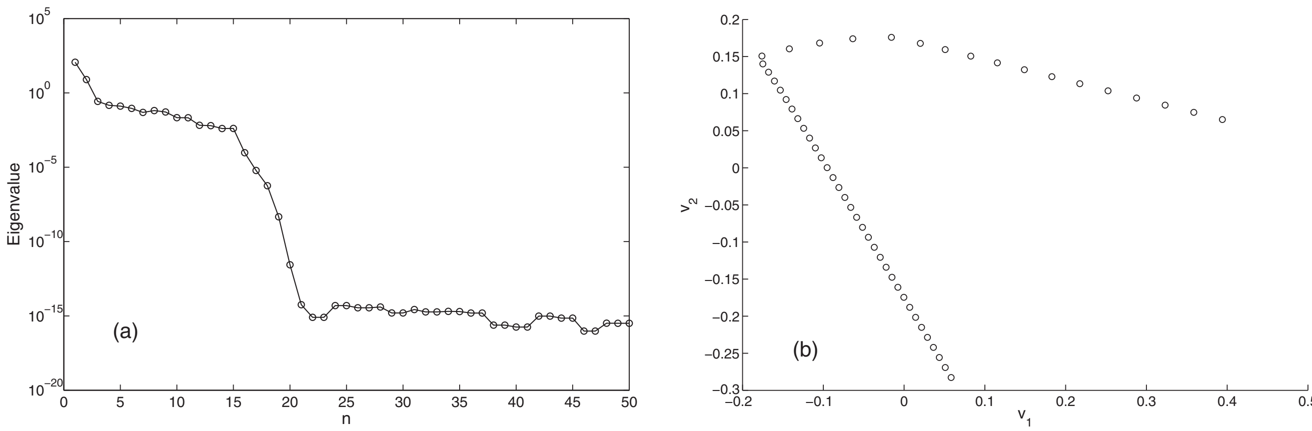

FIG. 4. Second case: (a) the eigenvalues of the embedding matrix in logarithmic scale; in (b) the first two eigenvectors represented in a phase-plane plot.

III. APPLICATIONS

In this section we present four illustrations of increasing complexity ranging from an exact idealized case to experimental data. In order to actually compute the Wasserstein distance matrix we refer to the technique presented in [10], where the optimal mass transfer problem is solved by a method based on the fact that optimal transport reduces to straight lines in Lagrangian coordinates.

A. Ideal vortex scattering

We consider two couples of counter-rotating ideal point vortices in the plane. The flow is incompressible and the vorticity is represented by four Dirac masses located at the vortex centers, so that the flow is irrotational almost everywhere. Under these hypotheses the flow is potential and the trajectories of the point vortices are obtained by the solution of a Hamiltonian dynamical system. The detailed derivation of the governing equations is found in [11].

The flow domain is $\mathbb{R}^2$ and the coordinates of the vortex cores are

$$x_a = r_1 \cos(\theta_1) \;\; y_a = r_1 \sin(\theta_1), \tag{30}$$

$$x_b = r_2 \cos(\theta_2) \;\; y_b = r_2 \sin(\theta_2), \tag{31}$$

$$x_c = r_1 \cos(\theta_1 + \pi) \;\; y_c = r_1 \sin(\theta_1 + \pi), \tag{32}$$

$$x_d = r_2 \cos(\theta_2 + \pi) \;\; y_d = r_2 \sin(\theta_2 + \pi), \tag{33}$$

where r_1, r_2, θ_1, and θ_2 are the only variables necessary to describe the interaction. They are initialized as follows:

$$r_1(0) = [l^2 + (1+\beta) f^2]^{1/2}, \tag{34}$$

$$r_2(0) = [l^2 + (1-\beta) f^2]^{1/2}, \tag{35}$$

$$\theta_1(0) = \arctan\left[\frac{(1+\beta)f}{l}\right], \tag{36}$$

$$\theta_2(0) = \arctan\left[\frac{(1-\beta)f}{l}\right], \tag{37}$$

where l, β, and f are three parameters that determine the distance of the dipoles, the relative distance of the

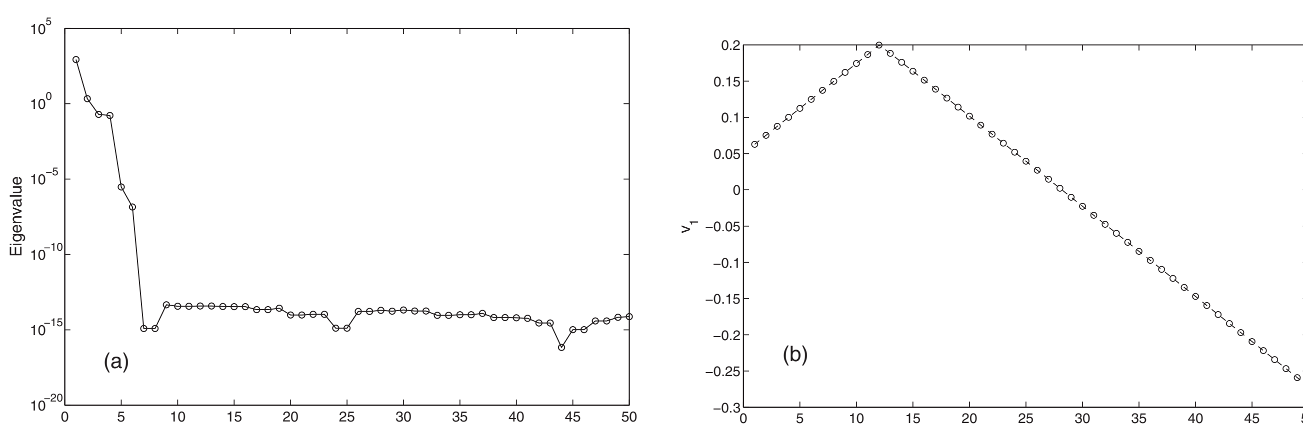

FIG. 5. Third case: (a) the eigenvalues of the embedding matrix in logarithmic scale; in (b) the first eigenvector.

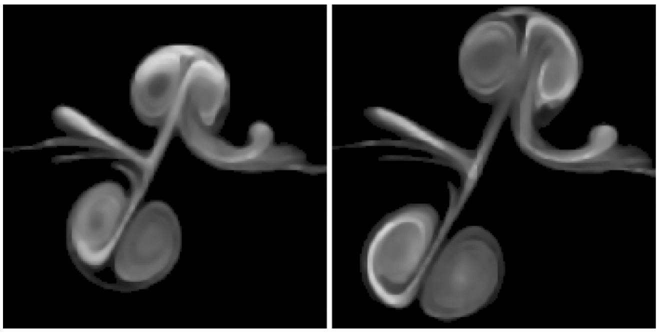

FIG. 6. Image of experimental vortex collision (courtesy of G. van Heijst). Two subsequent images visualizing rotational regions post collision. 100×100 pixel images.

counter-rotating vortices, and the offset of the dipole axis. The initial geometry of the system determines the nature of the scattering occurring between the dipoles. The ODEs describing the evolution are

$$\dot{r}_1 = -\frac{2\sin[2(\theta_1-\theta_2)]r_1 r_2^2}{\pi\{r_1^4 - 2\cos[2(\theta_1-\theta_2)]r_1^2 r_2^2 + r_2^4\}}, \tag{38}$$

$$\dot{r}_2 = -\frac{2\sin[2(\theta_1-\theta_2)]r_2 r_1^2}{\pi\{r_1^4 - 2\cos[2(\theta_1-\theta_2)]r_1^2 r_2^2 + r_2^4\}}, \tag{39}$$

$$\dot{\theta}_1 = \frac{3r_1^4 - 2\cos[2(\theta_1-\theta_2)]r_1^2 r_2^2 - r_2^4}{2\pi r_1^2\{r_1^4 - 2\cos[2(\theta_1-\theta_2)]r_1^2 r_2^2 + r_2^4\}}, \tag{40}$$

$$\dot{\theta}_2 = \frac{r_1^4 + 2\cos[2(\theta_1-\theta_2)]r_1^2 r_2^2 - 3r_2^4}{2\pi r_2^2\{r_1^4 - 2\cos[2(\theta_1-\theta_2)]r_1^2 r_2^2 + r_2^4\}}. \tag{41}$$

The equations of motion are integrated via an adaptive-step fourth-order Runge-Kutta scheme in the time interval [0,2.5]. In Fig. 2, three different situations are represented: (a) a scattering where the vortices keep their partner (the parameters used are $l = 1.5$, $\beta = 0.5$, $f = 0.25$); (b) a case where the vortices exchange their partner and escape with the counter-rotating vortex belonging to the other dipole ($l = 1.0$, $\beta = 0.75$, $f = 0.15$); (c) a weak interaction in which the dipoles simply move on (almost) straight lines ($l = 2.0$, $\beta = 0.15$, $f = 0.30$).

We consider the L^2 norm of vorticity (enstrophy) as the transported density ϱ. In this motion enstrophy is constant, so that we analyze the dynamics of four unitary Dirac masses. In this case, the Wasserstein distance between the time snapshots was computed by means of an exact combinatorial algorithm. For all the following cases 50 time frames were taken between initial and final time.

The embedding technique presented in the previous section was adopted. The spectrum of matrix B includes a few negative eigenvalues due to the fact that the distance is not Euclidean. They are small in modulus so that $B \approx B^+$. In Fig. 3 the eigenvalues of the embedding matrix are represented for the first case described (a). Only two eigenvalues are relevant in the approximation of the phenomenon. The corresponding eigenvectors are represented in a phase-plane plot. The circles represent the components of the eigenvectors and can be associated to the time frames. Two directions that represent the optimal transports occurring before and after the interaction can be observed. The points which are not aligned represents the snapshots of the enstrophy configurations occurring during the interaction. For case (b) (see Fig. 4) the spectrum of the embedding matrix is similar to that obtained for the first case: two eigenvalues emerge. The phase plot of the first two eigenvectors shows that the vortex interaction is quite different, but again two main transport directions corresponding to the dynamics before and after the interaction are present.

The third case (see Fig. 5) is different from the others. The interaction is weak and the resulting motion is practically an optimal transport. This third case may be considered as a perturbation of a single optimal transport. Indeed, in Fig. 5(a) the plot of the eigenvalues confirms that only one eigenvalue is important. The plot of the corresponding eigenvector in Fig. 5(b) shows that most of the snapshots are aligned, that is, they may be obtained by nonlinear interpolation (i.e., by transport) of the barycentral density via a unique optimal transport.

In this simple example the comparison with standard POD is straightforward. For the second and the third cases [Figs. 2(b) and 2(c)] the autocorrelation matrix (i.e., the matrix of scalar products of the snapshots) is the identity matrix. Hence, no reduction can be provided by using POD. For the first case [Fig. 2(a)], the trajectories intersect, so that the autocorrelation matrix may not be diagonal for some specific samplings. However, only few extra diagonal elements appear, so that, even in this case, no signal reduction is possible.

Although this is a conceptual test case, there are real flows that can be described by this model. In Fig. 6 we present two subsequent images of an experimental vortex collision

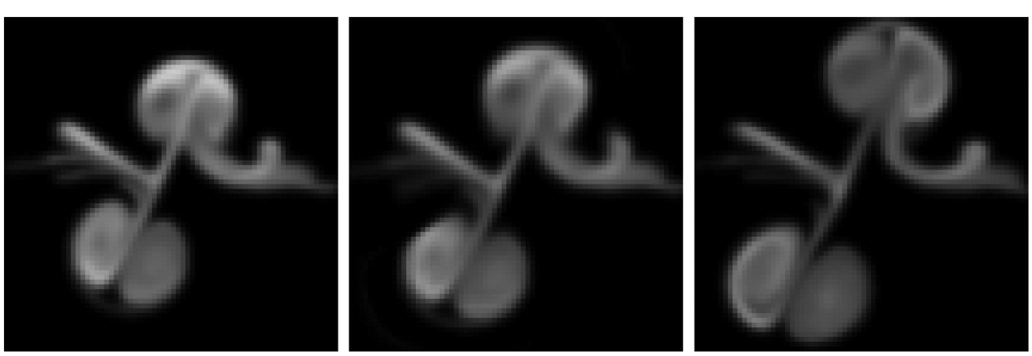

FIG. 7. Smoothed densities. The leftmost and rightmost figures correspond to initial time and final time, respectively. In the middle, the nonlinear interpolation at time $T = 1/2$. 100×100 pixel images.

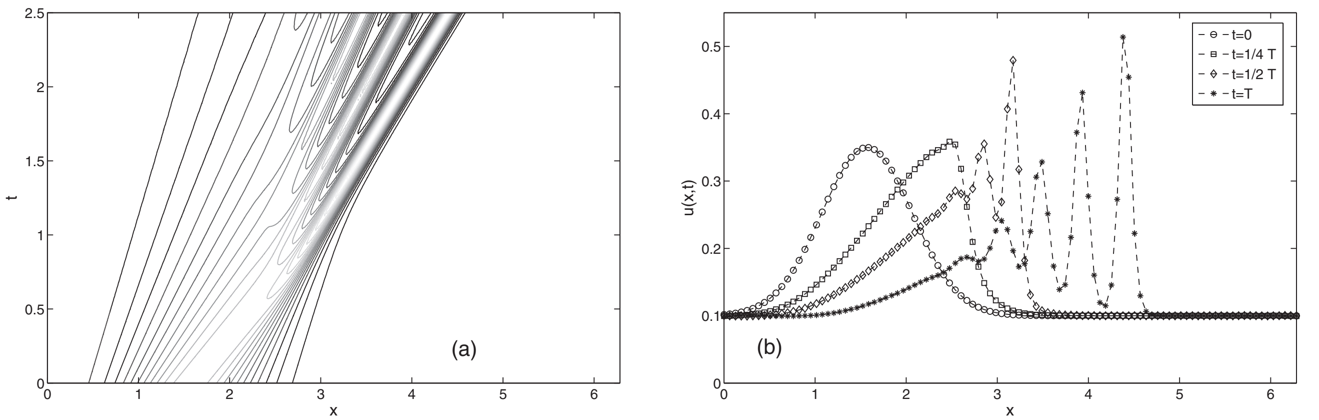

FIG. 8. Solution of the KdV model: (a) contour of x-t diagram, 20 values between minimum and maximum; (b) solution at different times, where $T = 2.5$.

obtained in a configuration that is close to the ideal case presented (courtesy of G. van Heijst) [12]. These images correspond to a postcollision dipole evolution. In order to perform an optimal transport analysis, we took the normalized modulus of the color intensity (green or red) as the density to be mapped ϱ.

In order to find one advection mode, we took these two postinteraction images and solved an optimal transport problem between them. Thanks to this mode, an intermediate image of the dipole was reconstructed. In particular, the density associated to initial time [see Fig. 7(a)] was mapped into that at final time [in Fig. 7(c)]. Then the density associated to $X_{\mathrm{int}} = \xi + 1/2 v_0$ is computed and shown in Fig. 7(b). Since the initial images are noisy, we have smoothed them with a Gaussian filter to numerically solve the transport problem. The reconstructed image is clearly not a linear interpolation of the initial and final images and qualitatively models an intermediate configuration between the initial and final one.

B. Waves on shallow water surfaces

Waves on shallow water surfaces can be modeled by the one-dimensional Korteveg–de-Vries equation. It is an interesting test case because in this model transport and dispersion can be modulated. The model equation reads

$$\partial_t u + u \partial_x u \; + \gamma \partial_{xxx} u = 0, \tag{42}$$

where $u(x,t)$ is the wave elevation at time $t \in [0,2.5]$ and position $x \in [0,2\pi]$, $\gamma = 1e-3$ is the dispersion parameter. Periodic boundary conditions are imposed. The initial condition is $u(x,0) = u_0(x)$ and for the present case is taken as

$$u_0(x) = 0.1 + \exp\left\{-2\left(x - \frac{\pi}{2}\right)^2\right\}. \tag{43}$$

This equation was numerically integrated using a spectral discretization in space (256 Fourier modes), and a second order Cranck-Nicholson method with 10^3 steps in time.

The preserved measure is in this case the energy of the signal. Let $e = u^2$, then it can be proved that $\forall t$,

$$E(t) = \int_0^{2\pi} e(x,t)\, dx = E(0) = \int_0^{2\pi} u_0(x)^2\, dx. \tag{44}$$

Solutions of this model, displayed in Fig. 8, show transport and dispersion. In particular, as γ is small, in the first part of the evolution the system evolves as an inviscid Burgers model [Fig. 8(b)]. When a shock tends to form, the third derivative norm becomes large and dispersion makes the solution brake in several waves, with different characteristic velocities.

For this case, a comparison between POD and the proposed technique is carried out. We take set of 24 snapshots of the solution energy, normalized by its integral (which is constant) between the time $t = 0$ and the time $t = T = 2.5$.

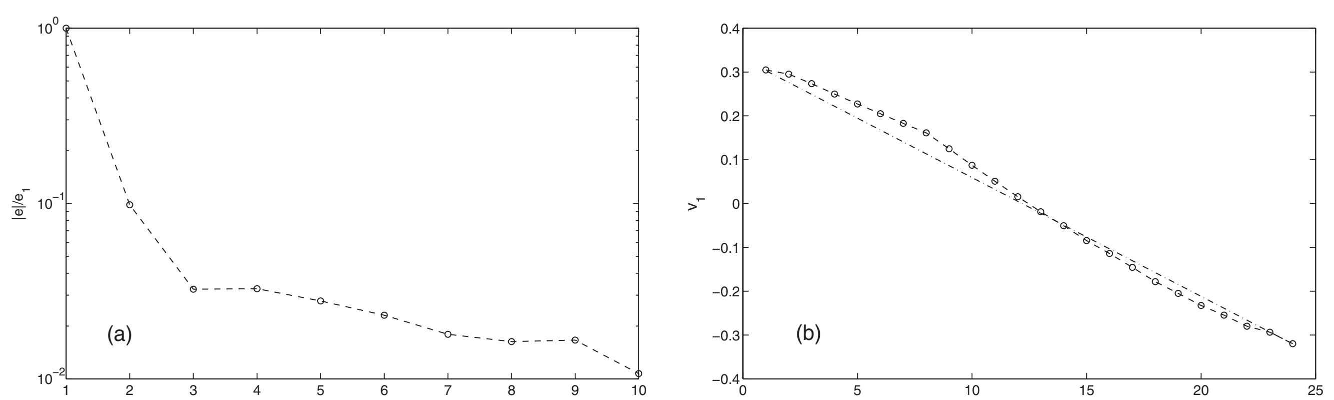

FIG. 9. Embedding matrix analysis: (a) first ten normalized eigenvalues in modulus; (b) components of the first eigenvector.

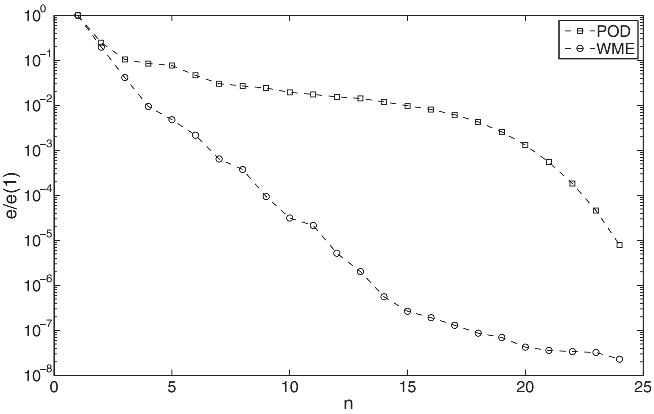

FIG. 10. Comparison between standard POD and the POD of the residuals pushed back. Normalized eigenvalues of the autocorrelation matrix

Let us compute the advection modes defined by means of Wasserstein distance. We computed the optimal transport between all the possible couples of snapshots and then we formed the embedding matrix as described in the previous sections. The eigenvalues and eigenvectors of this matrix are shown in Fig. 9(a). The absolute value of the first ten eigenvalues is plotted, normalized with the value of the first one: one dominant eigenvalue appears. In Fig. 9(b) the corresponding eigenvector is plotted for each snapshot.

This advection mode may be defined using the straight line connecting the first snapshot with the last one [see Fig. 9(b)], as it is a good interpolant of all the snapshots. This is by definition the optimal mapping that transports the first snapshot, $e(x,0)$, into the last one $e(x,T)$. Let us denote by $X_1(\xi,t)$ this mapping.

The second step of the procedure consists in computing the residuals of this representation. The snapshots $e(x,t_i)$ are mapped back to the initial configuration defined by $X_1(\xi,t)$. The differences between the solution snapshots pushed back and $e(x,0) = e_0(\xi)$ is computed by

$$R_i = R(\xi,t_i) = e(X_1(\xi,t_i),t_i)\partial_\xi X_1 - e_0(\xi), \tag{45}$$

where $e(X_1(\xi,t_i),t_i)\partial_\xi X_1$ are the snapshots $e_i(x,t_i)$ pushed back by the advection mode. These residuals are then decomposed in the reference configuration by means of a standard POD analysis. Let us compare the results of this analysis with that of the POD applied to the original set of snapshots. In Fig. 10 the normalized spectrum of the autocorrelation matrix is shown for the standard POD applied to the snapshots of the energy, and for the POD applied to the residuals pushed back. The eigenvalues cascade for the latter is steeper, i.e., a smaller number of modes is necessary for given representation error.

In Fig. 11(a) the advection mode U_1 is represented as function of $X_1(\xi,0) = \xi$. The Lagrangian coordinate used to push back the residuals is $X_1(\xi,t) = \xi + tU_1(\xi)$. In Figs. 11(b) and 11(c) the first and second residual mode is represented as a function of ξ. Let us remark that these modes have significant variations in the portion of the domain where the initial energy distribution varies. Let us compare these modes with the classical POD modes for the energy distribution, represented in Fig. 12. The POD modes are quite different from the residual modes: they are global and their support

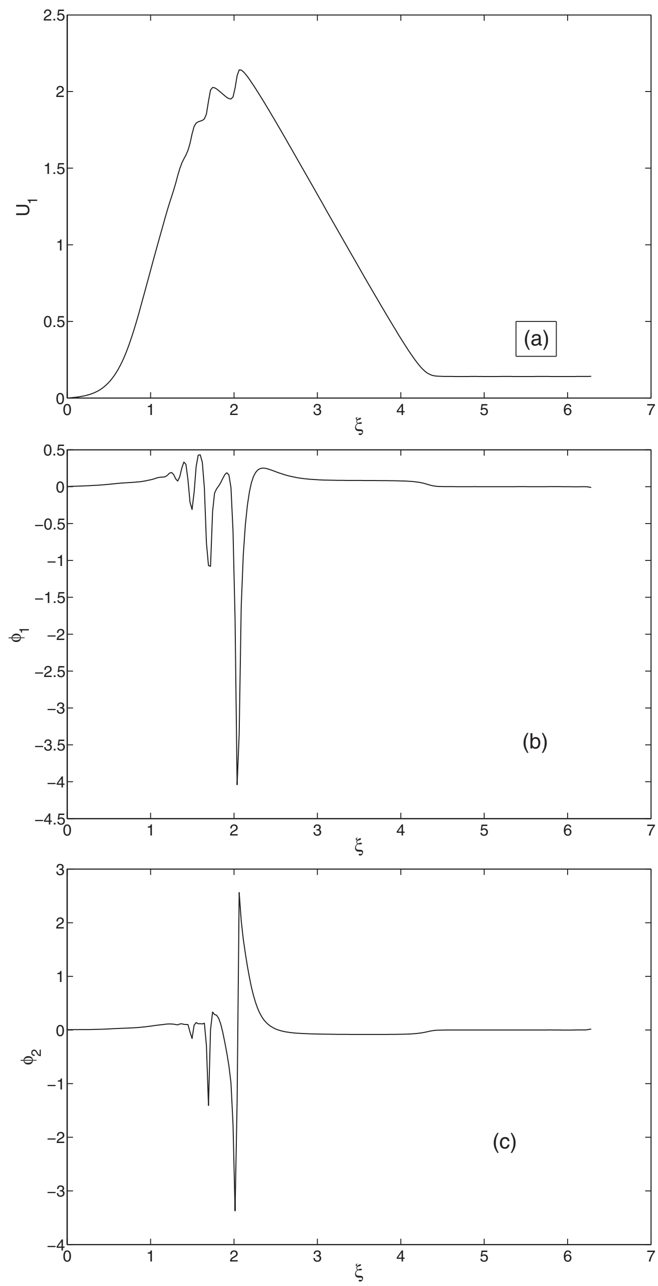

FIG. 11. Advection modes expansion for KdV model: (a) advection mode; (b) first mode of the residuals; (c) second mode of the residuals.

approximately extends to the whole domain. We compare now the reconstruction of the snapshots using the advection mode decomposition (AMD) and POD. The same number of modes is used for both techniques. Hence, for the POD reconstruction we will use one additional mode compared to the number of residual modes. This allows a fair comparison because for the advection mode decomposition we also have (in this case) one transport.

Three different reconstructions are considered using four, six, and ten POD modes respectively. In Fig. 13 the L^2 normalized errors are plotted as a function of the snapshot number for POD and advection mode decomposition. In all

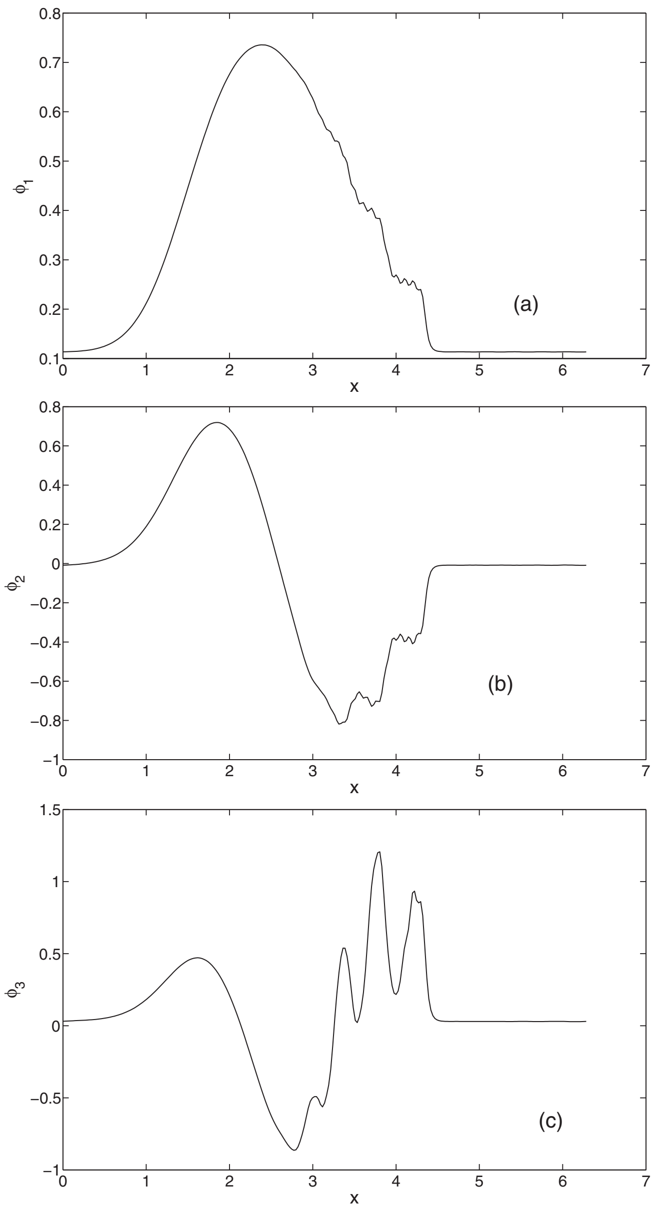

FIG. 12. POD modes for the normalized kinetic energy: (a) first mode; (b) second mode; (c) third mode.

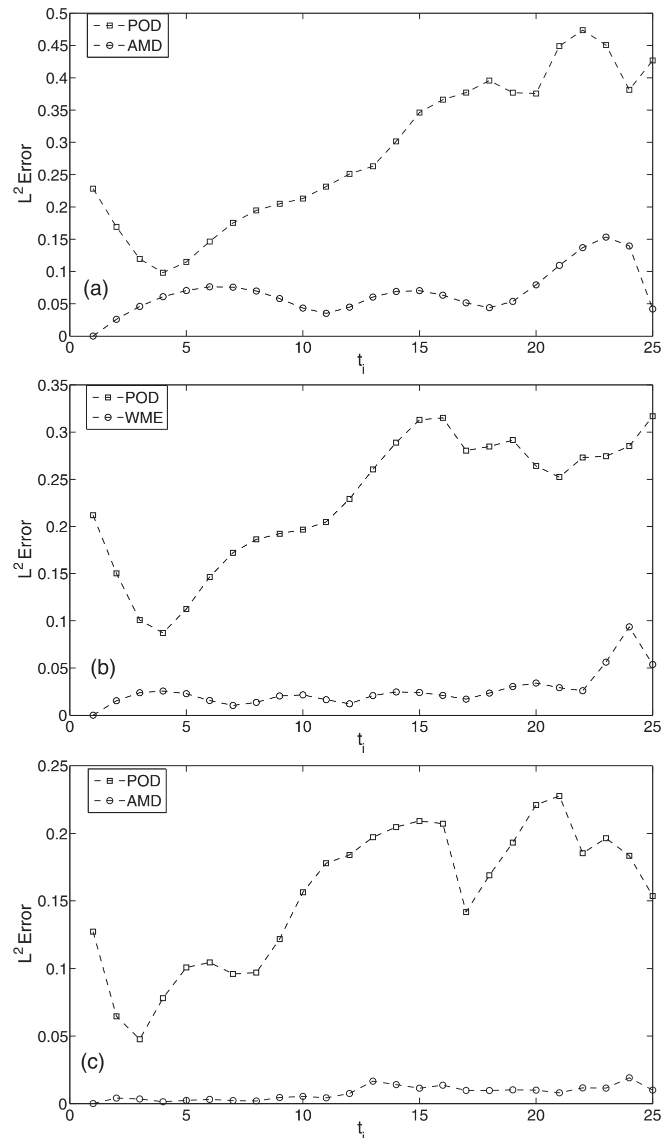

FIG. 13. L^2 errors as a function of the snapshot number: (a) four modes; (b) six modes; (c) ten modes.

three cases the advection mode decomposition shows an error that is significantly smaller with respect to that of POD. Also, it tends to diminish faster as the number of modes is increased. This could be anticipated from the spectrum decay. The reconstructions in the physical space for both methods are compared to the snapshot for which the representation given by advection mode decomposition is worst, that is $n = 23$.

When few modes are used, like in Fig. 14(a), POD is not able to reproduce the peaks that characterize the solution. In the cases shown in Figs. 14(b) and 14(c) POD provides a nonphysical solution due to its essentially oscillatory nature: the reconstructed kinetic energy is negative in a few regions of the domain. The advection mode decomposition in Fig. 14(b) is such that all the key features of the solution are well reproduced. In Fig. 14(c) the agreement is even improved.

C. Hurricane Dean

We consider the satellite images of the Caribbean Sea between the 17th and 22nd of August 2007 showing the trajectory of hurricane Dean. The images are based on data from the NOAA archive [13] to get the location and time line of the storm. The images were generated by a NASA Goddard Space Center application[14]. Again, only ten snapshots are considered. In this case, the density is simply defined as the normalized grey scale image. The time sampling was 6 h, so that the time interval between the first snapshot and the last one is $T = 54$ h. In Fig. 15 three images are shown, at time $t = 0, T/2, T$. The resolution is 512×256.

Here we concentrate on the possibility of using advection mode decomposition and POD to estimate a subsequent image not included in the initial database. The most energetic POD mode obtained from the ten snapshots database is shown in Fig. 16(a): it is the average of the snapshots. The average position of the hurricane may be inferred from this

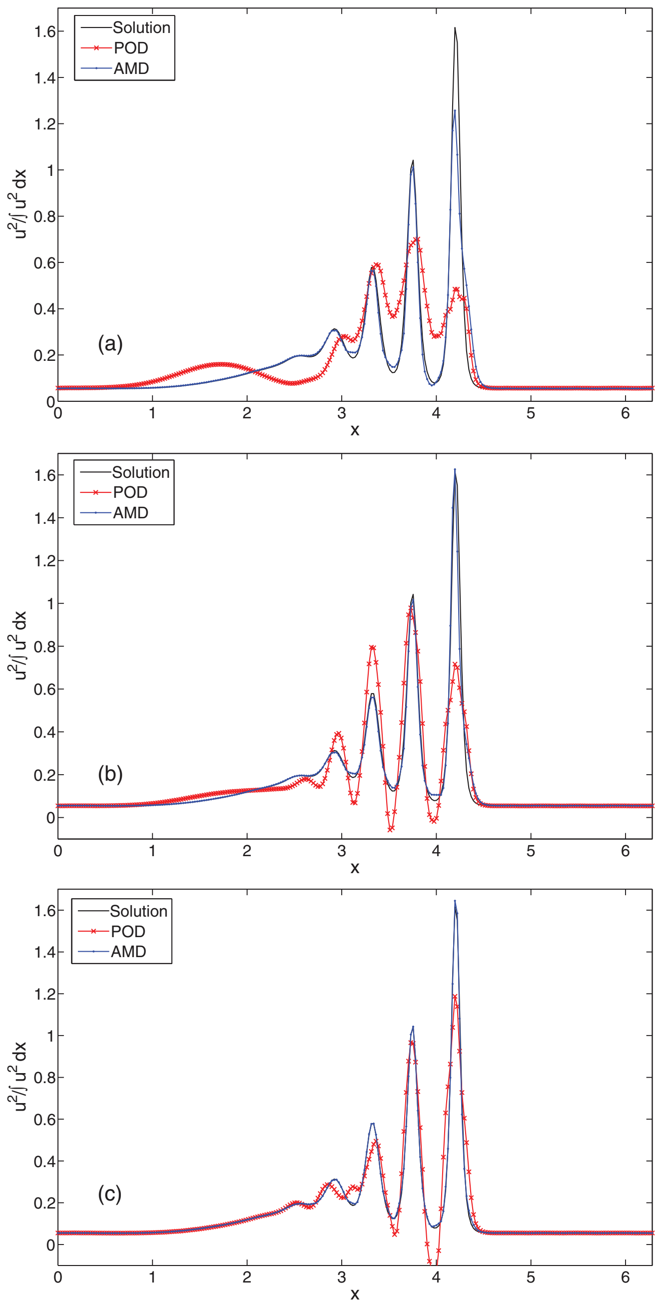

FIG. 14. (Color online) Solid line is the solution, dotted line is the advection mode decomposition, cross line is POD representation when (a) four modes, (b) six modes, (c) ten modes are used.

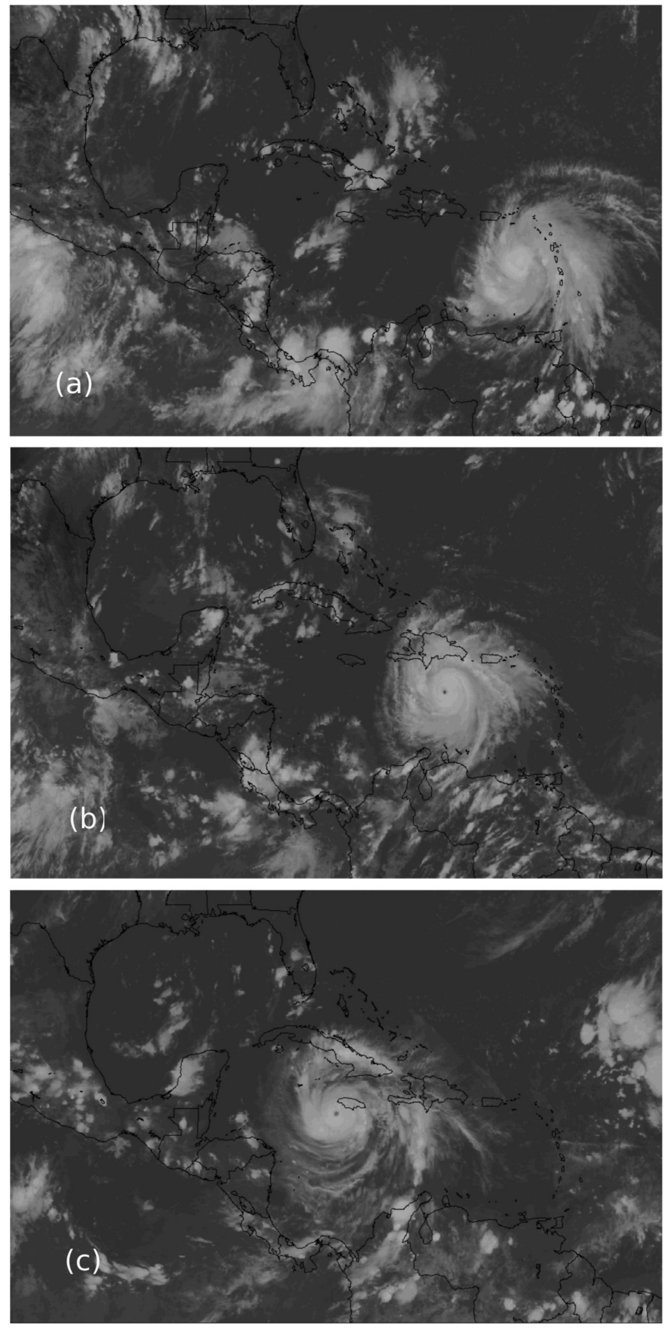

FIG. 15. Images of hurricane Dean at (a) $t = 0$, (b) $t = 27$ h, and (c) 54 h.

picture. The other modes, see Figs. 16(b) and 16(c), render the hurricane motion through global oscillating modes. No particular structure is visible in these modes. This is consistent with the fact that POD tends to the Fourier basis when it represents transported structures.

As for advection mode decomposition, a set of $N_s - 1$ mapping is considered ($N_s = 10$ is the number of snapshots). This allows us to map the snapshot ϱ_n into ϱ_{n+1}. This set may be used to define, by numerical integration, a Lagrangian coordinate for the system. Let Φ_n be the mapping that transports ϱ_n into $\varrho_n + 1$. The following holds:

$$X(\xi,t_n) = \int_0^{t_n} v \, d\tau = \int_0^{t_n} \nabla\Phi \, d\tau = Q(\xi,\Phi_n), \qquad (46)$$

where X is the Lagrangian coordinate and Q is a quadrature formula. In this case a second order Adams-Bashforth scheme was used to integrate the mappings. Let us remark that X is not the Lagrangian coordinate of the physical system, but it is a mapping that allows us to recover its state starting from the initial condition thanks to the Wasserstein map between each image. In Fig. 17 the Lagrangian coordinate is represented at times $t = 0, T/2, T$. The deformation of the space is more

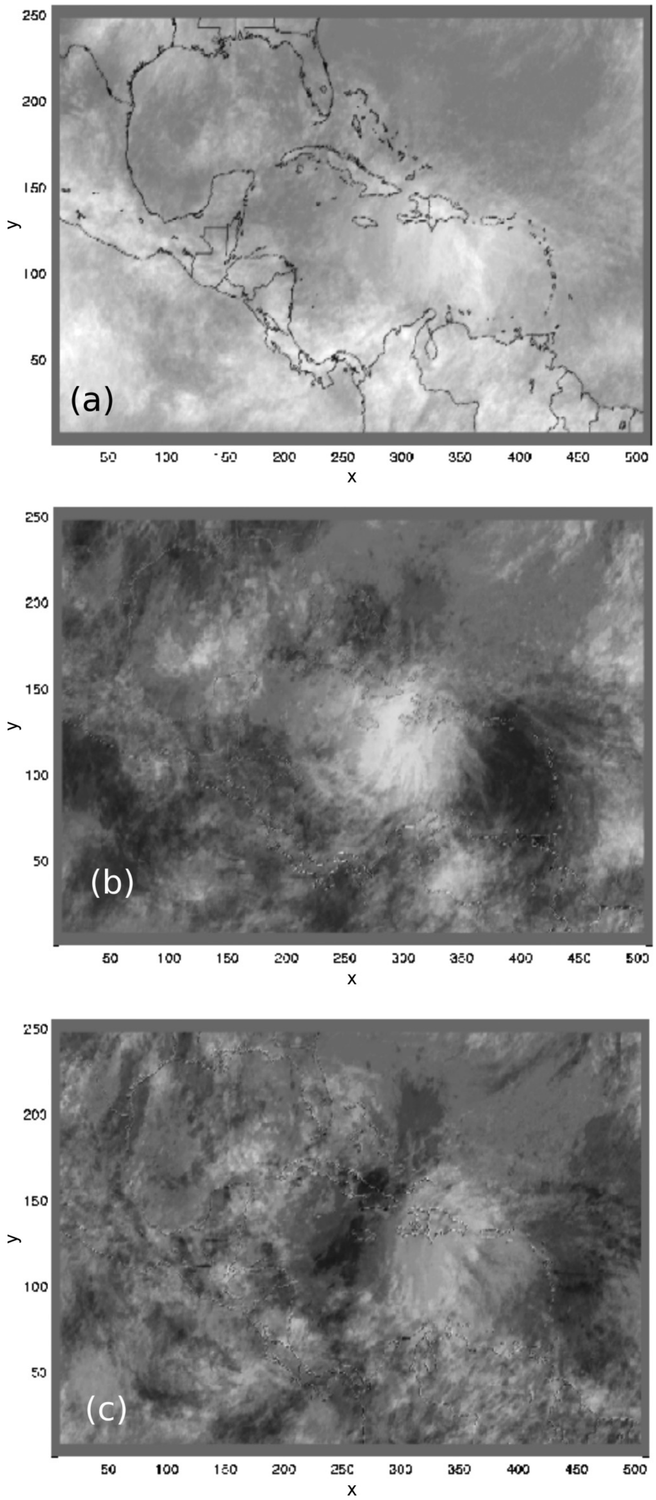

FIG. 16. POD modes: (a) first mode, (b) second mode, (c) third mode.

intense around the hurricane [see for instance Figs. 17(b) and 17(c)]. This is due to the fact that its motion is more coherent than that of all the other structures. Optimal transport allows us to highlight this feature in a straightforward manner.

We computed the advection modes. These modes represent potentials that suitably combined allow us to map the first image of the sequence to all the others. With three advection

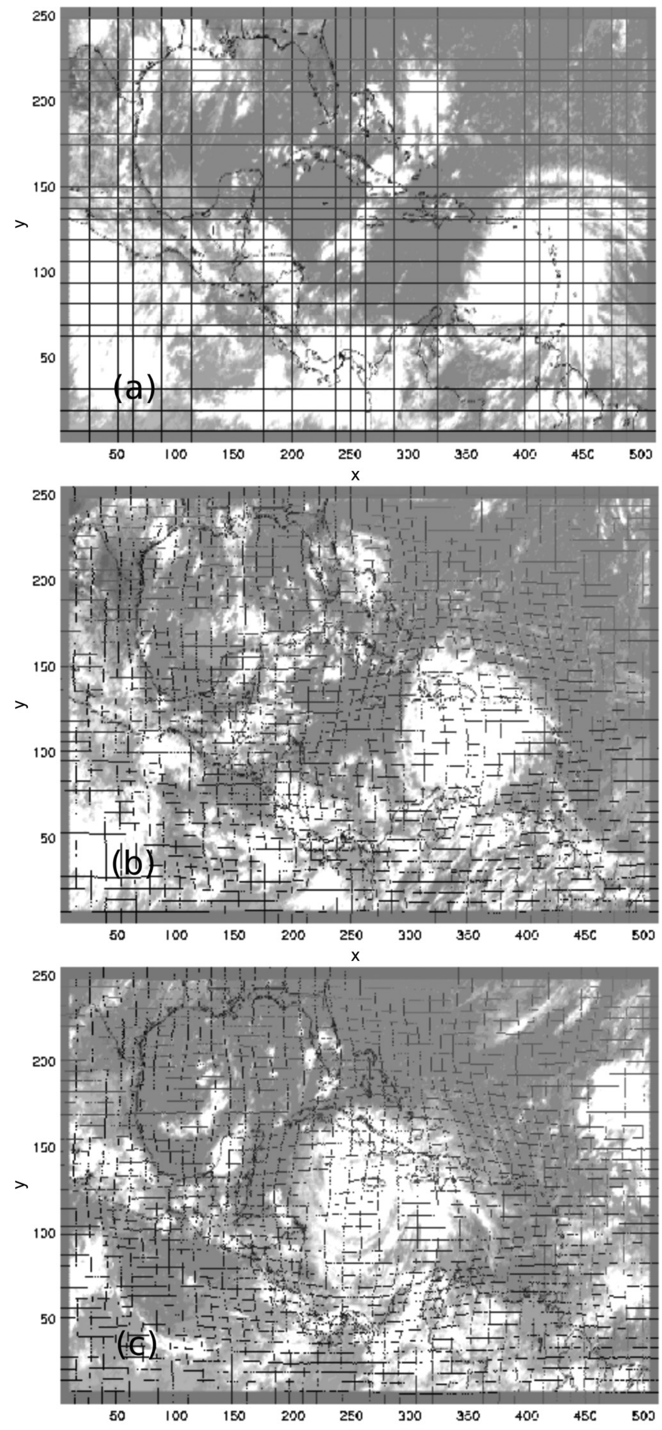

FIG. 17. Lagrangian Coordinate at time a) $t = 0$ b) $t = T/2$ c) $t = T$.

modes, we can recover all the images with an error which is about 9% in norm L^2 of the gray scale.

We considered a subsequent hurricane image at time $T^* = 60$ h not included in the database to compute the POD modes and the advection modes. For POD representation, a simple problem of approximation is investigated, i.e., how accurately the new snapshot is represented using the POD modes computed using the database whose last snapshot is at $T = 54h$.

The error of the reconstruction of this last image based on POD modes is about 16% using all the POD modes and does not vary significantly with the number of the modes used.

The approach based on Wasserstein distance allows us to extrapolate the regularized Lagrangian coordinate in a natural way. The discrete points (computed as explained above) $X(\xi,t_n)$, $n = 1,\dots,10$, are used to estimate $X(\xi,t_{n+1})$ via a standard polynomial extrapolation. The error between the extrapolated Lagrangian coordinate and that computed using the novel datum at $T = 60$ h differs by 0.0108 in norm L^2. This means that the position of the hurricane is extrapolated with an error that is at most of 1%.

IV. CONCLUSION

In this paper we have proposed an advection based modal decomposition. It exploits the Wasserstein distance to define an advection mode hierarchy that describes the main features of advection. Additional features are included by using a POD mode expansion of the residual in a reference domain. When dealing with systems in which transport is the leading phenomenon, this method provides an efficient and meaningful low-order representation. This has been shown by contrasting the results of this approach to standard POD analysis for different cases ranging from idealized vortex motion, to actual hurricane data.

APPENDIX: NORMALIZATION OF THE EMBEDDING

Let us suppose that the densities ϱ_i are taken by uniformly sampling in time an optimal transport between ϱ_0 and ϱ_{N_s-1}. In this case, X_i, mapping ϱ_0 into ϱ_i is written by interpolation (see [8]):

$$X_i = \xi + i\Delta t \nabla_\xi \Phi(\xi), \tag{A1}$$

where Δt is the sampling time, and Φ is a (almost everywhere) convex potential. In this particular case, all the densities are aligned on a one-dimensional subspace of the Wasserstein space, since they belong to the same optimal transport. Hence, we expect that only one eigenvalue of matrix B is different from 0.

The squared Wasserstein distance between the ith and the jth sample is

$$\mathcal{W}^2(\varrho_i,\varrho_j) = \int_{\Omega_i} \varrho_i(\eta)|X_{ij}(\eta) - \eta|^2 d\eta, \tag{A2}$$

where $X_{ij}(\eta)$ is the optimal mapping between ϱ_i and ϱ_j. For these particular mappings the elements of the matrix have the form

$$\mathcal{D}_{ij} = \mathcal{W}^2(\varrho_i,\varrho_j) = \frac{C}{N_s^2}(i-j)^2, \tag{A3}$$

where C is a constant, representing the squared Wasserstein distance (i.e., twice the kinetic energy) of the unique mapping linking all the snapshots. The time at which the last snapshot is taken is taken to be $T = 1$.

Let us consider the matrix $\tilde{\mathcal{D}} = (i-j)^2$, $\tilde{\mathcal{D}} \in \mathbb{R}^{n\times n}$ and prove that the associated embedding matrix B has only one zero eigenvalue and that this value is $\lambda = \frac{n(n+1)(n-1)}{12}$.

The elements of B are computed using two standard results in finite series:

$$\sum_j^n j = \frac{n(n+1)}{2}, \quad \sum_j^n j^2 = \frac{n(n+1)(2n+1)}{6}. \tag{A4}$$

By performing all the matrix vector products and exploiting the projector properties we have

$$-(2\mathcal{B})_{ij} = (n+1)(i+j) - 2ij - \frac{(n+1)^2}{2}$$
$$\Rightarrow \mathcal{B}_{ij} = \frac{(n+1)^2}{4} + ij - \frac{(n+1)}{2}(i+j). \tag{A5}$$

Let $k = \frac{n+1}{2}$. The expression for the entries of B can be recast as follows:

$$\mathcal{B}_{ij} = k^2 - k(i+j) + ij \ \Rightarrow\ \mathcal{B}_{ij} = (k-i)(k-j). \tag{A6}$$

The relation written above states that B is the tensor product of a unique vector, whose components are $y_i = (k-i)$. This is sufficient to prove the first point. Let us now explicitly compute the only nonzero eigenvalue λ. Again, the results on finite series are used, leading to

$$\lambda = \sum_i^n (k-i)^2 = \frac{n(n+1)(n-1)}{12}. \tag{A7}$$

The normalization condition for the generic $B \in \mathbb{R}^{N_s\times N_s}$ is then

$$\overline{B} = \frac{B}{\mathcal{N}} = -\frac{6N_s}{N_s^2 - 1} JDJ. \tag{A8}$$

[1] P. Holmes, J. L. Lumley, and G. Berkooz, *Turbulence, Coherent Structures, Dynamical Systems and Symmetry*, 1st ed. (Cambridge University Press, Cambridge, England,1996).

[2] L. Sirovich, Contemp. Math. **99**, 277 (1989).

[3] B. Galletti, C. H. Bruneau, L. Zannetti, and A. Iollo, J. Fluid Mech. **503**, 161 (1999).

[4] I. Mezić, Nonlinear Dyn. **41**, 309 (2005).

[5] C. W. Rowley, I. Mezić, S. Bagheri, P. Schlatter, and D. S. Henningson, J. Fluid Mech. **641**, 115 (2009).

[6] P. Schmid, J. Fluid Mech. **656**, 5 (2010).

[7] C. Villani, *Topics in Optimal Transportation*, 1st ed. (American Mathematical Society, Providence, 2003).

[8] J.-D. Benamou and Y. Brenier, Numer. Mat. **84**, 375 (2000).

[9] M. Muskulus and S. Verduyn-Lunel, Physica D **240**, 45 (2011).

[10] A. Iollo and D. Lombardi, J. Comput. Phys. **230**, 3430 (2011).

[11] V. V. Meleshko and M. Y. Konstantinov, *Vortex Dynamics and Chaotic Phenomena*, 1st ed. (World Scientific, Singapore, 2002).

[12] G. J. F. van Heijst and J. B. Flor, Nature (London) **340**, 212 (1989).

[13] http://www.aoc.noaa.gov/archive.htm

[14] http://disc.sci.gsfc.nasa.gov/daac-bin/